ACS Energy LETTERS

Cite This: ACS Energy Lett. 2019, 4, 1954−1960

http://pubs.acs.org/journal/aelccp

LETTER

Enhanced Open-Circuit Voltage of Wide-Bandgap Perovskite Photovoltaics by Using Alloyed $(FA_{1-x}Cs_x)Pb(I_{1-x}Br_x)_3$ Quantum Dots

Mokshin Suri,[†,‡] Abhijit Hazarika,[†] Bryon W. Larson,[†] Qian Zhao,[†,§] Marta Vallés-Pelarda,[∥,†] Timothy D. Siegler,[‡] Michael K. Abney,[‡] Andrew J. Ferguson,[†] Brian A. Korgel,*[,‡] and Joseph M. Luther*[,†]

[†]National Renewable Energy Laboratory, Golden, Colorado 80401, United States

[‡]McKetta Department of Chemical Engineering and Texas Materials Institute, The University of Texas at Austin, Austin, Texas 78712-1062, United States

[§]College of Chemistry, Nankai University, Tianjin 300071, China

[∥]Institute of Advanced Materials (INAM), Universitat Jaume I, Avenida de Vicent Sos Baynat, s/n, 12006 Castelló de la Plana, Castellón, Spain

Supporting Information

ABSTRACT: We report a detailed study on $APbX_3$ (A = formamidinium (FA^+), Cs^+; X = I^-, Br^-) perovskite quantum dots (PQDs) with combined A- and X-site alloying that exhibits both a wide bandgap and high open-circuit voltage (V_{oc}) for the application of a potential top cell in tandem junction photovoltaic (PV) devices. The nanocrystal alloying affords control over the optical bandgap and is readily achieved by solution-phase cation and anion exchange between previously synthesized $FAPbI_3$ and $CsPbBr_3$ PQDs. Increasing only the Br^- content of the PQDs widens the bandgap but results in shorter carrier lifetimes and associated V_{oc} losses in devices. These deleterious effects can be mitigated by replacing Cs^+ with FA^+, resulting in wide-bandgap PQD absorbers with improved charge-carrier mobility and PVs with higher V_{oc}. Although further device optimization is required, these results demonstrate the potential of $FA_{1-x}Cs_xPb(I_{1-x}Br_x)_3$ PQDs for wide-bandgap perovskite PVs with high V_{oc}.

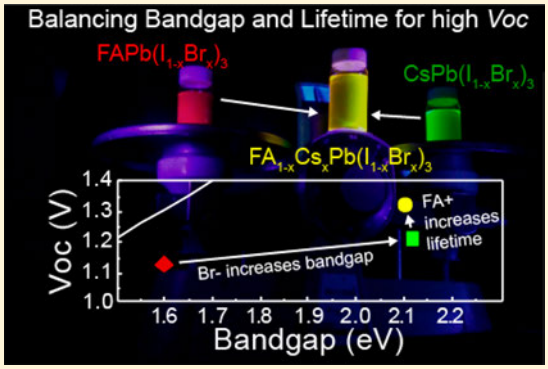

The search for high-efficiency, wide-bandgap absorber materials that can be implemented as a top cell in a tandem architecture to boost the overall efficiency of existing commercial photovoltaic (PV) devices (e.g., Si, CIGS, CdTe) remains a challenge.[1−10] The tunable nature of perovskite (ABX_3) absorbers, coupled with their impressive optoelectronic performance and amenability to low-cost deposition techniques, identifies them as a promising candidate for such applications.[11−19]

Although triple-cation bulk perovskite absorbers—$Cs_x(FA_yMA_{(1-y)})_{(1-x)}Pb(I_zBr_{(1-z)})_3$—exhibit impressive solar light to electricity power conversion efficiencies (PCEs), with the current PCE record at 24.2%, their bandgap (1.55−1.60 eV) is too narrow for use as the top cell in multijunction PVs.[20,21] Tuning halide composition on the X site enables wider optical bandgaps but has not led to the expected subsequent increase in V_{oc}, and mixed-halide bulk perovskites often suffer from photoinduced halide segregation and crystal phase instability that leads to device degradation.[12,13,22−26] Perovskite quantum dots (PQDs) provide a route to circumvent these structural instabilities, with the added benefit that they afford additional tunability of the optical and electronic properties (by tuning the QD size and composition).[12,13,15,22−24,27,28] For instance, mixed-cation PQDs with the composition $FA_{1-x}Cs_xPbI_3$ exhibit broader compositional tunability (wider x range) than bulk phase $FA_{1-x}Cs_xPbI_3$.[29] $FA_{1-x}Cs_xPbI_3$ PQD PVs achieve V_{oc}'s that approach 90% of the radiative limit (similar to single-crystal III−V PVs, i.e., $GaInP_2$), surpassing the V_{oc} of bulk perovskite PVs with similar composition in the bandgap range of 1.55−1.77 eV, as shown in Figure S1.[29−31] Taken together, these observations suggest that PQDs may provide an ideal solution for inexpensive, high-

Received: May 13, 2019
Accepted: July 16, 2019
Published: July 16, 2019

DOI: 10.1021/acsenergylett.9b01030
ACS Energy Lett. 2019, 4, 1954−1960

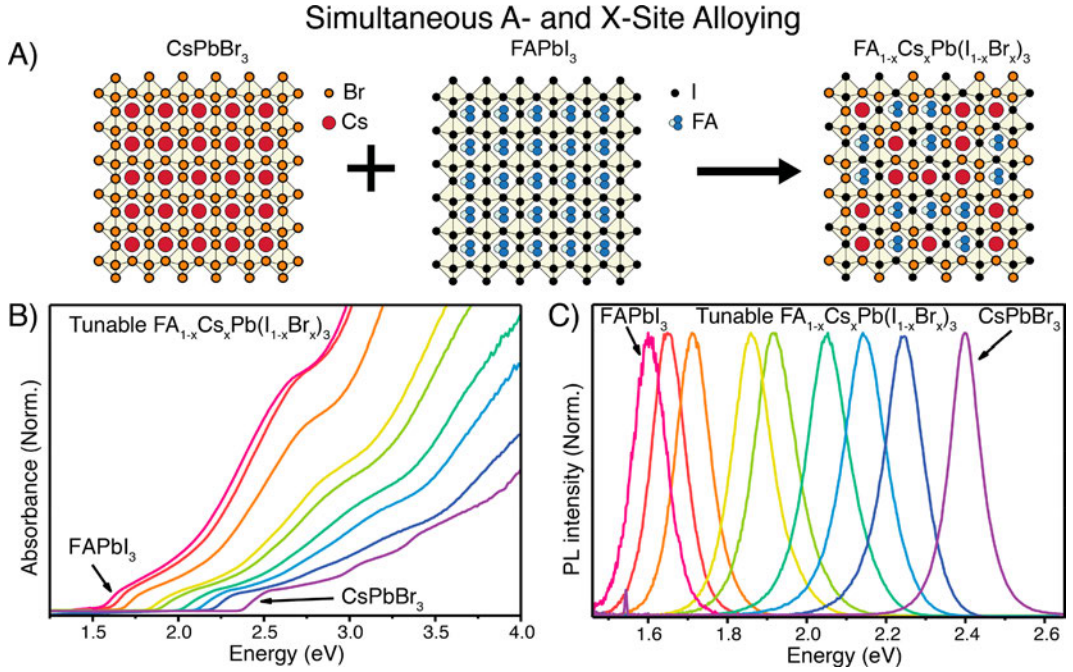

Figure 1. (A) Crystal models showing the ion-exchange process used to generate alloyed PQDs. $FA_{1-x}Cs_xPb(I_{1-x}Br_x)_3$ PQDs are generated when dispersions of $CsPbBr_3$ and $FAPbI_3$ PQDs are mixed at 70 °C. Room-temperature (B) absorbance and (C) PL emission spectra of PQDs with varying $FA_{1-x}Cs_xPb(I_{1-x}Br_x)_3$ composition dispersed in octane (excitation wavelength of 400 nm).

performance, wide-bandgap top cell absorber layers in multijunction PVs.

Wider-bandgap PQDs (bandgap higher than 1.77 eV), thus far, do not show the same low V_{oc} losses as those with bandgaps between 1.55 and 1.77 eV. Compositionally increasing the bandgap of PQDs with Br^- incorporation results in a decreasing voltage fraction in PVs from 0.9 to 0.63 (in this work, we define voltage fraction as device V_{oc}/maximum V_{oc} based on the device bandgap as determined by EQE onset).[22,31,32] Thus, finding solutions to this unexpected voltage loss would be beneficial for the wide-bandgap top cell in multijunction PVs.

Here, we show that combined A- and X-site alloying of wide-bandgap $FA_{1-x}Cs_xPb(I_{1-x}Br_x)_3$ PQDs can provide increased device V_{oc} as compared to $CsPb(I_{1-x}Br_x)_3$ and $FAPb(I_{1-x}Br_x)_3$ PQDs at bandgaps wider than 1.8 eV. The addition of Br in $CsPb(I_{1-x}Br_x)_3$ PQDs—typically used to increase the bandgap—leads to a significantly decreased photoluminescence (PL) lifetime and correlates with lost V_{oc} in PVs made from these PQDs.[22,32,33] To counter this, FA^+ was added in addition to Br^- to develop long PL lifetime, wide-bandgap materials. This co-alloying strategy was found to improve charge transport in PQD films and reduce the voltage loss in PVs with E_g > 1.8 eV.

To generate the PQDs of such complicated composition, two simple compositions were first synthesized and alloyed using an ion-exchange reaction. Figure 1A illustrates the ion exchange between $CsPbBr_3$ and $FAPbI_3$ PQDs used to generate $FA_{1-x}Cs_xPb(I_{1-x}Br_x)_3$ PQDs. $CsPbBr_3$ and $FAPbI_3$ PQDs were prepared using previously reported recipes.[12,29] By mixing dispersions of $FAPbI_3$ and $CsPbBr_3$ PQDs at 70 °C, rapid and efficient compositional alloying occurred. This enabled PQDs with a wide tunability of the bandgap from 1.55 to 2.40 eV to be obtained from similar starting materials simply by controlling the relative amount of $CsPbBr_3$ to $FAPbI_3$ in the ion-exchange reaction. Figure 1B,C shows absorbance and PL spectra of PQDs generated from the same $CsPbBr_3$ and $FAPbI_3$ PQD starting materials. The nanocrystals retain a relatively narrow size distribution comparable to that of the starting materials.

We first highlight the deleterious effects of Br^- incorporation in single A-site PQD PVs by using colloidal PQDs with bandgaps ranging between 1.8 and 1.94 eV containing only Cs^+ on the A-site. Unlike PQDs of $FA_{1-x}Cs_xPb(I_{1-x}Br_x)_3$ composition, $CsPb(I_{1-x}Br_x)_3$ and $FAPb(I_{1-x}Br_x)_3$ PQDs were synthesized using previously reported methods of single-pot direct synthesis using controlled ratios of Pb-halide salts.[12] Figure 2A shows a scanning electron microscopy (SEM) image of a cross-sectioned $CsPbI_3$ PQD PV. The PQD solar cells were fabricated using previously reported methods.[34−37] For ideal removal of the oleate ligands, it is especially important to maintain an ambient environment that exhibits 15−25% relative humidity (RH) during the ligand-exchange procedure performed after deposition of the nanocrystals.[35] Figure 2B shows the device responses of $CsPbI_3$ PQD PVs and $CsPb(I_{1-x}Br_x)_3$ PQD PVs with Br^- alloying to widen the bandgap. The $CsPbI_3$ PQD PV exhibits a PCE of ∼14% (reverse scan). The $CsPb(I_{1-x}Br_x)_3$ PQD PVs have lower device efficiency, which is expected based on the widened bandgap and corresponding reduced light absorption; however, they also show a decrease in the V_{oc} contrary to the expectations for the widened bandgap with increased Br^- content. A noticeable drop in fill factor (FF) is also observed with increasing Br^- incorporation, which suggests increased series resistance in the device possibly originating from nonideal contact layers in the device structure. Full device metrics for the devices shown in Figure 2B are provided in Table S1 as Supporting Information.

Figure 2C,D shows solution-phase PL emission spectra and solution-phase time-resolved photoluminescence (TRPL) measurements on $CsPbI_3$ PQDs compared to $CsPb(I_{1-x}Br_x)_3$ PQDs with 8 and 13% Br^- compositions. The compositions of

DOI: 10.1021/acsenergylett.9b01030
ACS Energy Lett. 2019, 4, 1954−1960

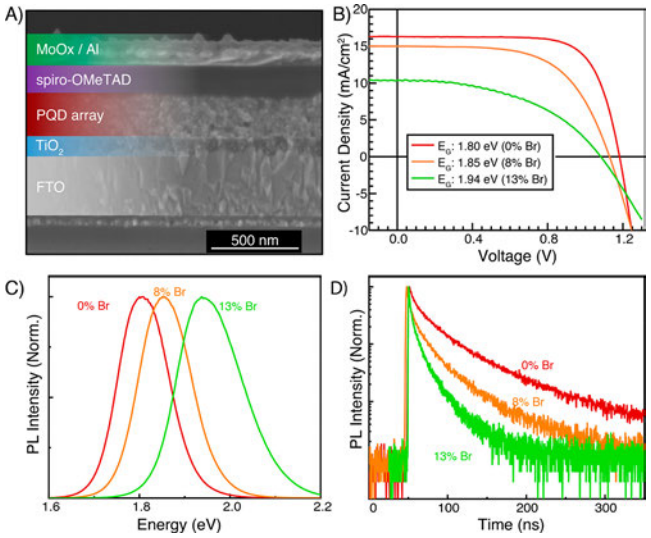

Figure 2. (A) SEM image of a cross-sectioned $CsPbI_3$ PQD PV device. (B) J/V curves of $CsPb(I_{1-x}Br_x)_3$ PQD PVs with varying Br^- composition and bandgap. Note that the reported bandgaps correspond to the PL peak energies of solution-phase PQDs that were used to prepare the PVs. The device bandgap of PQD PVs is typically red-shifted by 0.05−0.1 eV with respect to solution-phase PQDs, due to ligand exchanges during device fabrication, which induce electronic coupling.[17,33] (C) Room-temperature normalized PL emission spectra of the colloidal PQDs used to fabricate devices tested in (B). The excitation wavelength was 400 nm. (D) Time-resolved PL transients of the $CsPb(I_{1-x}Br_x)_3$ PQDs used to make the devices from panel (B). The excitation wavelength is 442 nm, and the emission is collected at the PL peak position.

all PQD samples in this work are estimated using Vegard's Law.[38] As expected, the increase in the Br^-/I^- ratio results in a hypsochromic shift of the PL spectrum, but the mixed halide systems also exhibit broadening of the emission spectrum, which may be related to an increase in the polydispersity of the PQDs or a nonuniform halide composition within the ensemble. We find that $CsPb(I_{1-x}Br_x)_3$ PQDs show significantly reduced PL lifetime compared to the $CsPbI_3$ PQDs. On the basis of previous reports, we believe that increased Br^- composition leads to higher PL quantum yield and decreased PL lifetime, which suggests that shorter radiative lifetimes are intrinsic to Br-rich PQDs.[11,13,15,17] See Supporting Information Figure S2 for a plot summarizing the radiative lifetimes versus bandgap and Br^- content of PQD samples. From the results in Figure 2, we hypothesize that increased bromine content in PQDs leads to a decreased PL lifetime and that the PL lifetime of colloidal PQDs is related to PQD device performance, especially the deteriorating V_{oc} performance at wide bandgaps, as discussed above.

To test this hypothesis, TRPL measurements of several colloidal PQD compositions ($CsPb(I_{1-x}Br_x)_3$, $FAPb(I_{1-x}Br_x)_3$, and $FA_{1-x}Cs_xPb(I_{1-x}Br_x)_3$) were conducted using a streak-camera system that records spectral- and time-dependent emission data. Figure 3A shows two-dimensional solution-phase TRPL data for $CsPbI_3$ colloidal PQDs, and the red dashed box in Figure 3A shows the region of the response that is integrated to produce a TRPL transient decay curve. The inset in Figure 3A shows the actual transient that is extracted from the streak-camera response. While the TRPL measurements were performed in the solution phase, we believe that the reduced PL lifetime of colloidal $CsPb(I_{1-x}Br_x)_3$ PQDs is at

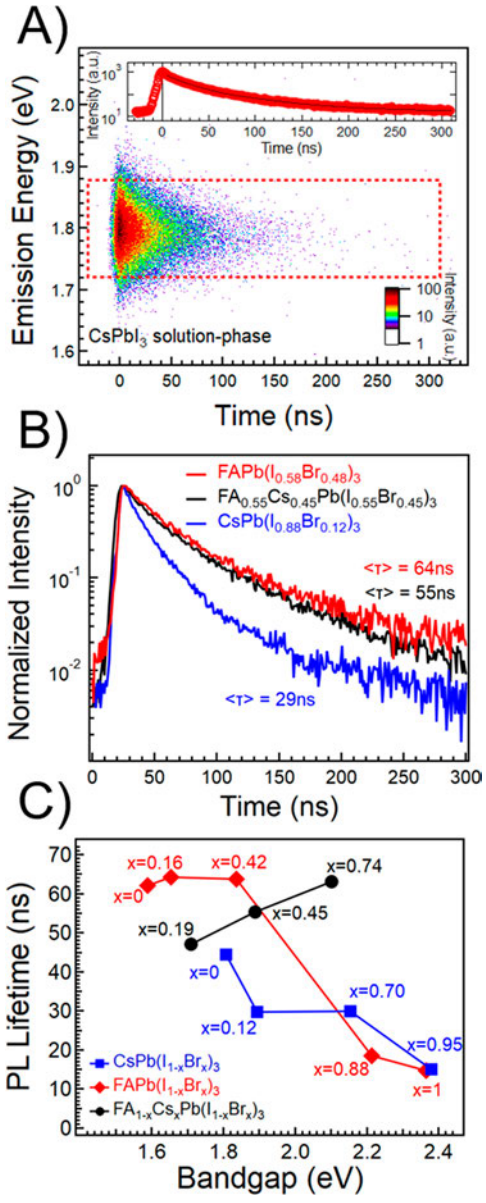

Figure 3. (A) Two-dimensional spectrotemporal solution-phase TRPL data of $CsPbI_3$ PQDs, measured using a streak-camera. The red rectangle represents the portion of the trace that was integrated to construct an intensity versus decay-time transient. (B) Solution-phase TRPL transients of $CsPb(I_{1-x}Br_x)_3$, $FAPb(I_{1-x}Br_x)_3$, and $FA_{1-x}Cs_xPb(I_{1-x}Br_x)_3$ PQDs with bandgap energies of ca. 1.9 eV. (These PQD compositions are estimated using Vegard's Law based on the PL peak energy.[38]) (C) Intensity-averaged PL lifetime versus bandgap of all solution-phase PQD samples including $CsPb(I_{1-x}Br_x)_3$, $FAPb(I_{1-x}Br_x)_3$, and $FA_{1-x}Cs_xPb(I_{1-x}Br_x)_3$ PQDs. See Figure S2 for the estimated radiative lifetime component versus bandgap of each sample.

least partly related to the observed loss in device V_{oc}. To overcome this, we aimed to lengthen the PL lifetime of these PQDs through compositional alloying. While that challenge at face value is not so straightforward, it has been reported that $FAPbI_3$ QDs have a substantially longer PL lifetime than $CsPbI_3$, but unfortunately, replacing Cs^+ with FA^+ also lowers the bandgap.[39] We, therefore, hypothesized that by balancing the FA^+ to Cs^+ ratio, along with the Br^- to I^- ratio, we could engineer the PQDs to have an appropriate bandgap (from Br^+

DOI: 10.1021/acsenergylett.9b01030
ACS Energy Lett. 2019, 4, 1954−1960

incorporation) with lengthened PL lifetimes (from FA^+ incorporation). To test this specific hypothesis, we show in Figure 3B $CsPb(I_{1-x}Br_x)_3$, $FAPb(I_{1-x}Br_x)_3$, and $FA_{1-x}Cs_xPb(I_{1-x}Br_x)_3$ colloidal PQDs each with composition tuned to achieve a bandgap of approximately 1.9 eV. The TRPL transients show that FA^+ incorporation nearly doubles the lifetime from 29 to 55 ns for the FA^+/Cs^+ alloy sample or 64 ns for the sample with pure FA^+ on the A-site. Thus, in this case, the A-site mediated lengthening of the PL lifetime via FA^+ incorporation overcomes the expected X-site mediated PL lifetime shortening due to Br^- incorporation, and wide-bandgap PQDs with enhanced PL lifetimes are produced. Next, we aim to understand the general trends of how the lifetimes vary as a function of bandgap for each of these A-site conditions.

As shown in Figures 2D and 3B, the solution-phase intensity-averaged TRPL decays cannot be described by a single-exponential function. While the origin of this deviation from simple first-order decay kinetics is beyond the scope of this work, we analyze our data with a biexponential decay and compare the intensity-weighted average PL lifetimes (Figure 3C) of the $CsPb(I_{1-x}Br_x)_3$, $FAPb(I_{1-x}Br_x)_3$, and $FA_{1-x}Cs_xPb(I_{1-x}Br_x)_3$ PQDs as a function of bandgap. The intensity-weighted average PL lifetimes of the $CsPb(I_{1-x}Br_x)_3$ PQDs decreases significantly from about 45 to 15 ns across the compositional range, with a sharp decrease observed even for small Br^- contents (cf. Figure 2D). In contrast, the $FAPb(I_{1-x}Br_x)_3$ and $FA_{1-x}Cs_xPb(I_{1-x}Br_x)_3$ PQDs appear to be less sensitive to the substitution of I^- with Br^-. Single-A-site $FAPb(I_{1-x}Br_x)_3$ PQDs exhibit similar lifetimes of >60 ns until the bandgap exceeds 1.8 eV (Br^- content of 42%) where the lifetime drops precipitously to 15 ns, similar to the average lifetimes observed for the single-cation Cs-containing PQDs. The mixed-A-site $FA_{1-x}Cs_xPb(I_{1-x}Br_x)_3$ PQDs, on the other hand, exhibit PL lifetimes that actually increase with bandgap energy and reach 65 ns for a bandgap of 2.1 eV. To our knowledge, this increase in PL lifetime with increasing bandgap for the $FA_{1-x}Cs_xPb(I_{1-x}Br_x)_3$ composition is unique among PQDs. The full set of TRPL decay transient data and fitting parameters are provided as Supporting Information in Figure S3 and Table S2.

To explore the impact of the observed colloidal-optoelectronic properties of the PQDs on their PV performance, solar cells were fabricated with $CsPb(I_{1-x}Br_x)_3$, $FAPb(I_{1-x}Br_x)_3$, and $FA_{1-x}Cs_xPb(I_{1-x}Br_x)_3$ PQDs with bandgaps ranging from 1.55 to 2.04 eV. Figure 4A plots the V_{oc} of over 150 PQD PVs with 10 different compositions across a wide alloy space and bandgap regime. By displaying results from a large sample set, we are able to determine which composition of PQDs provides the most promise for use as wide-bandgap top cells in tandem devices. Of the PQD devices, those with A-site alloying of FA^+ and Cs^+ exhibit the highest V_{oc} at bandgaps wider than 1.8 eV. This trend is especially noticeable at a bandgap of ~1.85 eV, where the V_{oc} increases by over 100 mV as the PQD composition is changed from $CsPb(I_{0.88}Br_{0.12})_3$ to $FAPb(I_{0.58}Br_{0.42})_3$ to $FA_{0.45}Cs_{0.55}Pb(I_{0.55}Br_{0.45})_3$. At a bandgap of ~2.04 eV, the maximum V_{oc} of the $FA_{1-x}Cs_xPb(I_{1-x}Br_x)_3$ PQD devices is about 100 mV higher than that of $CsPb(I_{1-x}Br_x)_3$ PQD PVs. Figure 4B shows a plot of the voltage fraction against the bandgap of the PQD PVs. The voltage fraction decreases with increasing Br^- incorporation and widening bandgap. The PVs of $FAPbI_3$ PQDs with a bandgap of 1.55 eV exhibit the highest voltage fraction of ~0.9, and the PL lifetime

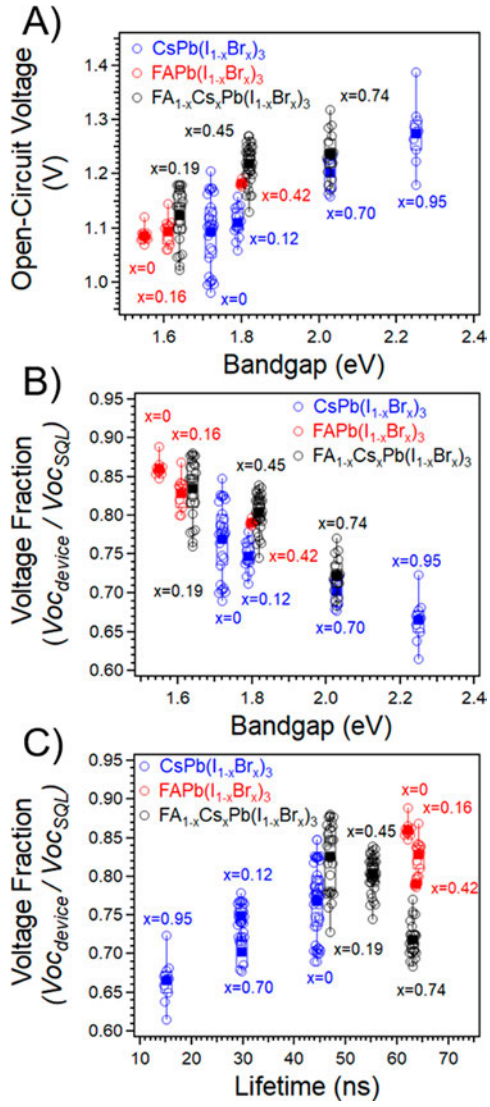

Figure 4. (A) V_{oc} versus bandgap of the full set of PQD PV samples. (B) Voltage fraction versus bandgap of the full data set of PQD PV samples. (C) Voltage fraction versus PL lifetime of the full data set of PQD PV samples. Full device metrics are provided as Supporting Information (Table S3).

of these PQDs is 62 ns. (Note, in Figure S1, we plot the voltage fraction of our PQD PVs against perovskite literature values to compare our results to the immense field of perovskite PVs and show the future promise of PQD PVs.)

To test our hypothesis that PQD PV voltage performance is correlated with the PL lifetime of colloidal PQDs, we plot the voltage fraction of PQD PVs versus the PL lifetime of solution-phase PQDs in Figure 4C. We observe that $CsPb(I_{1-x}Br_x)_3$ PQDs show a fairly direct relationship between the solution-phase PL lifetime and device voltage fraction. However, the voltage fraction of $FAPb(I_{1-x}Br_x)_3$ PQDs demonstrates a stronger compositional dependence; the voltage fraction of $FAPb(I_{1-x}Br_x)_3$ PQDs increases as the Br composition decreases. The fully alloyed PQDs ($FA_{1-x}Cs_xPb(I_{1-x}Br_x)_3$) generally exhibit a voltage fraction between 0.70 and 0.85, which is comparable to that of current, state-of-the-art bulk-phase $CsPbI_3$ devices (see Figure S1).[40] Although the A- and X-site alloying of $FA_{1-x}Cs_xPb(I_{1-x}Br_x)_3$ PQDs succeeded in producing devices with higher V_{oc} at wide bandgaps, the PCE

DOI: 10.1021/acsenergylett.9b01030
ACS Energy Lett. 2019, 4, 1954−1960

was still low, only 6% for a bandgap of 1.9 eV. We attribute these observations of lower PCE and the slight drop in voltage fraction of $FA_{1-x}Cs_xPb(I_{1-x}Br_x)_3$ PQD PVs, as "x" increases from 0.45 to 0.74, to poor charge transport in the PQD films and/or carrier extraction at the contact layers, which limits the J_{sc} and FF of the devices (see Supporting Information Table S3). We employed time-resolved microwave conductivity (TRMC) to determine how the A-site and X-site alloying influences the charge transport in the PQD films. The photoconductance, ΔG, extracted from the TRMC data can be related to a free-carrier yield-mobility product, $\phi\sum\mu$, which can be difficult to decompose into the individual contributions.[41,42] However, the large dielectric constant of PQDs and large PL lifetimes (>20 ns) allow us to make the assumption that each photon generates an unbound electron−hole pair on the 4 ns time scale of the laser pulse in the TRMC measurement (i.e., ϕ = 1), which simplifies the figure of merit to the sum of carrier mobilities.[42] Although we are able to make assumptions about the free-carrier yield, we cannot decouple the individual contributions of the electrons and holes to the photoconductance. Under such circumstances, the TRMC technique can be considered similar to other optical pump−probe techniques, except that the sum of the free-carrier mobilities, $\sum\mu$, now represents the absorption coefficient of the microwave probe. The transient photoconductance, $\Delta G(t)$, is therefore related to the number density, and associated kinetics, of the free electrons and holes in the PQD layer. Because we expect both carriers to contribute to the measured photoconductance and the carrier lifetime to be related to the likelihood of the carriers to be extracted in a functioning device, we suggest that the yield−mobility−tau product represents a reasonable metric to describe the free-carrier transport and dynamics (in fact, this quantity can be related to the carrier diffusion length).

Figure 5 shows the yield−mobility−tau products determined by TRMC of the ligand-exchanged PQD films on quartz substrates (the TRMC yield−mobilities and free-carrier lifetimes are also provided as Supporting Information Figure S4−S5). In all cases, the yield is assumed to be 1, meaning that we expect all charge carriers to diffuse, the mobility describes the sum of hole and electron mobility, and the carrier lifetime takes into consideration all holes and electrons. $CsPbI_3$ PQD films show the largest yield−mobility−tau product at ~500 × 10^{-9} cm^2/V. The yield−mobility−tau product decreases exponentially with increasing bandgap for single A-site PQDs, indicating that charge transport becomes less efficient with increasing Br composition. For $FA_{1-x}Cs_xPb(I_{1-x}Br_x)_3$ PQD films, the yield−mobility−tau product remains fairly stable across all three samples (~30−50 × 10^{-9} cm^2/V), and the 2.1 eV bandgap $FA_{1-x}Cs_xPb(I_{1-x}Br_x)_3$ PQD film leads to an enhanced yield−mobility−tau product over the single A-site PQD films with similar bandgap. Thus, at wide bandgaps, simultaneous alloying at the A- and X-sites leads to increased charge transport, but there is still room for improvement because the yield−mobility−tau products of $FA_{1-x}Cs_xPb(I_{1-x}Br_x)_3$ PQD films are an order of magnitude less than that of $CsPbI_3$ PQD films. Improvements in PQD synthesis, purification, and device fabrication are potential methods to improve charge transport in these films and improve the PCE.

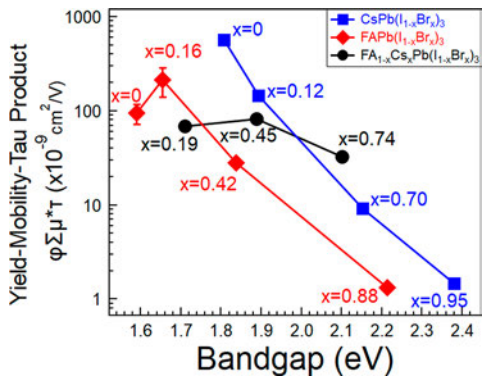

Figure 5. Yield−mobility−tau product determined by TRMC of $CsPb(I_{1-x}Br_x)_3$, $FAPb(I_{1-x}Br_x)_3$, and $FA_{1-x}Cs_xPb(I_{1-x}Br_x)_3$ PQD films on quartz substrates.

In conclusion, we show that the substitution of I^- for Br^- in metal halide PQDs results in faster electron−hole recombination, less efficient charge transport, and significant loss in device V_{oc} that hinders their performance in PQD PV devices. Simultaneous alloying on the A-site with Cs^+ and FA^+ to generate $FA_{1-x}Cs_xPb(I_{1-x}Br_x)_3$ PQDs counteracts these adverse effects of increased Br^- content. To our knowledge, $FA_{1-x}Cs_xPb(I_{1-x}Br_x)_3$ PQDs are the only PQDs to exhibit longer PL lifetimes with increased bandgap. $FA_{1-x}Cs_xPb(I_{1-x}Br_x)_3$ PQDs with bandgaps larger than 1.8 eV exhibit V_{oc} values nearly 100 mV higher than those of $CsPb(I_{1-x}Br_x)_3$ PQDs of similar bandgap. While further optimization of wide-bandgap PQD PVs is needed, these results suggest considerable promise for the continued improvement of wide-bandgap perovskite PV device layers needed for high-efficiency, low-cost multijunction solar cells.

■ ASSOCIATED CONTENT

Supporting Information

The Supporting Information is available free of charge on the ACS Publications website at DOI: 10.1021/acsenergylett.9b01030.

Experimental methods, characterizations, absorbance and photoluminescence of colloidal PQDs, TRPL transients including fitting parameters of colloidal PQDs, estimated radiative lifetimes for all colloidal PQD compositions, device metrics for PQD PVs in Figure 2, device metrics for all other PQD PVs for this study, TRMC lifetime of PQD thin films, and TRMC yield−mobility product of PQD thin films (PDF)

■ AUTHOR INFORMATION

Corresponding Authors

*E-mail: joey.luther@nrel.gov.
*E-mail: korgel@che.utexas.edu.

ORCID

Timothy D. Siegler: 0000-0001-6033-2232
Andrew J. Ferguson: 0000-0003-2544-1753
Brian A. Korgel: 0000-0001-6242-7526
Joseph M. Luther: 0000-0002-4054-8244

Notes

The authors declare no competing financial interest.

■ ACKNOWLEDGMENTS

This work was authored in part by the National Renewable Energy Laboratory, operated by Alliance for Sustainable Energy, LLC, for the U.S. Department of Energy (DOE)

DOI: 10.1021/acsenergylett.9b01030
ACS Energy Lett. 2019, 4, 1954−1960

under Contract No. DE-AC36-08GO28308. The QD synthesis was developed in the Laboratory Directed Research and Development program at NREL. The QD device fabrication acknowledges the Operational Energy Capability Improvement Fund of the Department of Defense. Time-resolved characterization at NREL was funded by the U.S. Department of Energy Office of Energy Efficiency and Renewable Energy Solar Energy Technologies Office. Funding for the work at The University of Texas was provided by the Robert A. Welch Foundation (F-1464) and the National Science Foundation through the Industry/University Cooperative Research Center (IUCRC) for Next Generation Photovoltaics (IIP-1540028 and IIP-1822206). M.S. would like to acknowledge the U.S. DOE, Office of Science, Office of Workforce Development for Teachers and Scientists, Science Undergraduate Laboratory Internship (SULI) Program for funding in 2017 and 2018. Q.Z. acknowledges fellowship support from the China Scholarship Council and Natural Science of Foundation China (21576140). M.V.-P. acknowledges Universitat Jaume I (UJI) through the FPI Fellowship Program (PREDOC/2017/40) and (E-2018-14) within the framework of Action 2 of the Mobility Program for Research Staff under the 2018 Research Promotion Plan. T.D.S. acknowledges United States government support under and awarded by the DoD, Air Force Office of Scientific Research, National Defense Science and Engineering Graduate (NDSEG) Fellowship, 32 CFR 168a. The views expressed in the article do not necessarily represent the views of the DOE or the U.S. Government.

REFERENCES

(1) McMeekin, D. P.; Sadoughi, G.; Rehman, W.; Eperon, G. E.; Saliba, M.; Hörantner, M. T.; Haghighirad, A.; Sakai, N.; Korte, L.; Rech, B.; et al. A Mixed-Cation Lead Mixed-Halide Perovskite Absorber for Tandem Solar Cells. *Science* **2016**, *351*, 151−155.

(2) Vos, A. D. Detailed Balance Limit of the Efficiency of Tandem Solar Cells. *J. Phys. D: Appl. Phys.* **1980**, *13*, 839−846.

(3) Karani, A.; Yang, L.; Bai, S.; Futscher, M. H.; Snaith, H. J.; Ehrler, B.; Greenham, N. C.; Di, D. Perovskite/Colloidal Quantum Dot Tandem Solar Cells: Theoretical Modeling and Monolithic Structure. *ACS Energy Lett.* **2018**, *3*, 869−874.

(4) Correa-Baena, J.-P.; Saliba, M.; Buonassisi, T.; Grätzel, M.; Abate, A.; Tress, W.; Hagfeldt, A. Promises and Challenges of Perovskite Solar Cells. *Science* **2017**, *358*, 739−744.

(5) Zhao, D.; Yu, Y.; Wang, C.; Liao, W.; Shrestha, N.; Grice, C. R.; Cimaroli, A. J.; Guan, L.; Ellingson, R. J.; Zhu, K.; et al. Low-Bandgap Mixed Tin−Lead Iodide Perovskite Absorbers with Long Carrier Lifetimes for All-Perovskite Tandem Solar Cells. *Nat. Energy* **2017**, *2*, 17018.

(6) Eperon, G. E.; Leijtens, T.; Bush, K. A.; Prasanna, R.; Green, T.; Wang, J. T.-W.; McMeekin, D. P.; Volonakis, G.; Milot, R. L.; May, R.; et al. Perovskite-Perovskite Tandem Photovoltaics with Optimized Band Gaps. *Science* **2016**, *354*, 861−865.

(7) Han, Q.; Hsieh, Y.-T.; Meng, L.; Wu, J.-L.; Sun, P.; Yao, E.-P.; Chang, S.-Y.; Bae, S.-H.; Kato, T.; Bermudez, V.; et al. High-Performance Perovskite/Cu(In,Ga)Se $_2$ Monolithic Tandem Solar Cells. *Science* **2018**, *361*, 904−908.

(8) Bush, K. A.; Palmstrom, A. F.; Yu, Z. J.; Boccard, M.; Cheacharoen, R.; Mailoa, J. P.; McMeekin, D. P.; Hoye, R. L. Z.; Bailie, C. D.; Leijtens, T.; et al. 23.6%-Efficient Monolithic Perovskite/Silicon Tandem Solar Cells with Improved Stability. *Nat. Energy* **2017**, *2*, 17009.

(9) Beal, R. E.; Slotcavage, D. J.; Leijtens, T.; Bowring, A. R.; Belisle, R. A.; Nguyen, W. H.; Burkhard, G. F.; Hoke, E. T.; McGehee, M. D. Cesium Lead Halide Perovskites with Improved Stability for Tandem Solar Cells. *J. Phys. Chem. Lett.* **2016**, *7*, 746−751.

(10) Siegler, T. D.; Shimpi, T. M.; Sampath, W. S.; Korgel, B. A. Development of Wide Bandgap Perovskites for Next-Generation Low-Cost CdTe Tandem Solar Cells. *Chem. Eng. Sci.* **2019**, *199*, 388−397.

(11) Becker, M. A.; Vaxenburg, R.; Nedelcu, G.; Sercel, P. C.; Shabaev, A.; Mehl, M. J.; Michopoulos, J. G.; Lambrakos, S. G.; Bernstein, N.; Lyons, J. L.; et al. Bright Triplet Excitons in Caesium Lead Halide Perovskites. *Nature* **2018**, *553*, 189−193.

(12) Protesescu, L.; Yakunin, S.; Bodnarchuk, M. I.; Krieg, F.; Caputo, R.; Hendon, C. H.; Yang, R. X.; Walsh, A.; Kovalenko, M. V. Nanocrystals of Cesium Lead Halide Perovskites ($CsPbX_3$, X = Cl, Br, and I): Novel Optoelectronic Materials Showing Bright Emission with Wide Color Gamut. *Nano Lett.* **2015**, *15*, 3692−3696.

(13) Akkerman, Q. A.; D'Innocenzo, V.; Accornero, S.; Scarpellini, A.; Petrozza, A.; Prato, M.; Manna, L. Tuning the Optical Properties of Cesium Lead Halide Perovskite Nanocrystals by Anion Exchange Reactions. *J. Am. Chem. Soc.* **2015**, *137*, 10276−10281.

(14) Pan, J.; Shang, Y.; Yin, J.; De Bastiani, M.; Peng, W.; Dursun, I.; Sinatra, L.; El-Zohry, A. M.; Hedhili, M. N.; Emwas, A.-H.; et al. Bidentate Ligand-Passivated $CsPbI_3$ Perovskite Nanocrystals for Stable Near-Unity Photoluminescence Quantum Yield and Efficient Red Light-Emitting Diodes. *J. Am. Chem. Soc.* **2018**, *140*, 562−565.

(15) Nedelcu, G.; Protesescu, L.; Yakunin, S.; Bodnarchuk, M. I.; Grotevent, M. J.; Kovalenko, M. V. Fast Anion-Exchange in Highly Luminescent Nanocrystals of Cesium Lead Halide Perovskites ($CsPbX_3$, X = Cl, Br, I). *Nano Lett.* **2015**, *15*, 5635−5640.

(16) Wu, L.; Zhong, Q.; Yang, D.; Chen, M.; Hu, H.; Pan, Q.; Liu, H.; Cao, M.; Xu, Y.; Sun, B.; et al. Improving the Stability and Size Tunability of Cesium Lead Halide Perovskite Nanocrystals Using Trioctylphosphine Oxide as the Capping Ligand. *Langmuir* **2017**, *33*, 12689−12696.

(17) Swarnkar, A.; Marshall, A. R.; Sanehira, E. M.; Chernomordik, B. D.; Moore, D. T.; Christians, J. A.; Chakrabarti, T.; Luther, J. M. Quantum Dot-Induced Phase Stabilization of α-CsPbI3 Perovskite for High-Efficiency Photovoltaics. *Science* **2016**, *354*, 92−95.

(18) Chen, Q.; Wu, J.; Ou, X.; Huang, B.; Almutlaq, J.; Zhumekenov, A. A.; Guan, X.; Han, S.; Liang, L.; Yi, Z.; et al. All-Inorganic Perovskite Nanocrystal Scintillators. *Nature* **2018**, *561*, 88−93.

(19) Talapin, D. V.; Lee, J.-S.; Kovalenko, M. V.; Shevchenko, E. V. Prospects of Colloidal Nanocrystals for Electronic and Optoelectronic Applications. *Chem. Rev.* **2010**, *110*, 389−458.

(20) Saliba, M.; Matsui, T.; Seo, J.-Y.; Domanski, K.; Correa-Baena, J.-P.; Nazeeruddin, M. K.; Zakeeruddin, S. M.; Tress, W.; Abate, A.; Hagfeldt, A.; et al. Cesium-Containing Triple Cation Perovskite Solar Cells: Improved Stability, Reproducibility and High Efficiency. *Energy Environ. Sci.* **2016**, *9*, 1989−1997.

(21) NREL. Best Research-Cell Efficiencies. https://www.nrel.gov/pv/cell-efficiency.html (accessed June 17, 2019).

(22) Christodoulou, S.; Di Stasio, F.; Pradhan, S.; Stavrinadis, A.; Konstantatos, G. High-Open-Circuit-Voltage Solar Cells Based on Bright Mixed-Halide $CsPbBrI_2$ Perovskite Nanocrystals Synthesized under Ambient Air Conditions. *J. Phys. Chem. C* **2018**, *122*, 7621−7626.

(23) Gualdrón-Reyes, A. F.; Yoon, S. J.; Barea, E. M.; Agouram, S.; Muñoz-Sanjosé, V.; Meléndez, Á. M.; Niño-Gómez, M. E.; Mora-Seró, I. Controlling the Phase Segregation in Mixed Halide Perovskites through Nanocrystal Size. *ACS Energy Lett.* **2019**, *4*, 54−62.

(24) Wang, X.; Ling, Y.; Lian, X.; Xin, Y.; Dhungana, K. B.; Perez-Orive, F.; Knox, J.; Chen, Z.; Zhou, Y.; Beery, D.; et al. Suppressed Phase Separation of Mixed-Halide Perovskites Confined in Endotaxial Matrices. *Nat. Commun.* **2019**, *10*, 695.

(25) Slotcavage, D. J.; Karunadasa, H. I.; McGehee, M. D. Light-Induced Phase Segregation in Halide-Perovskite Absorbers. *ACS Energy Lett.* **2016**, *1*, 1199−1205.

(26) Zeng, Q.; Zhang, X.; Feng, X.; Lu, S.; Chen, Z.; Yong, X.; Redfern, S. A. T.; Wei, H.; Wang, H.; Shen, H.; et al. Polymer-Passivated Inorganic Cesium Lead Mixed-Halide Perovskites for

DOI: 10.1021/acsenergylett.9b01030
ACS Energy Lett. 2019, 4, 1954−1960

Stable and Efficient Solar Cells with High Open-Circuit Voltage over 1.3 V. *Adv. Mater.* **2018**, *30*, 1705393.
(27) Hoffman, J. B.; Zaiats, G.; Wappes, I.; Kamat, P. V. $CsPbBr_3$ Solar Cells: Controlled Film Growth through Layer-by-Layer Quantum Dot Deposition. *Chem. Mater.* **2017**, *29*, 9767−9774.
(28) Creutz, S. E.; Crites, E. N.; De Siena, M. C.; Gamelin, D. R. Anion Exchange in Cesium Lead Halide Perovskite Nanocrystals and Thin Films Using Trimethylsilyl Halide Reagents. *Chem. Mater.* **2018**, *30*, 4887−4891.
(29) Hazarika, A.; Zhao, Q.; Gaulding, E. A.; Christians, J. A.; Dou, B.; Marshall, A. R.; Moot, T.; Berry, J. J.; Johnson, J. C.; Luther, J. M. Perovskite Quantum Dot Photovoltaic Materials beyond the Reach of Thin Films: Full-Range Tuning of A-Site Cation Composition. *ACS Nano* **2018**, *12*, 10327−10337.
(30) Cariou, R.; Benick, J.; Beutel, P.; Razek, N.; Flötgen, C.; Hermle, M.; Lackner, D.; Glunz, S. W.; Bett, A. W.; Wimplinger, M.; et al. Monolithic Two-Terminal III−V//Si Triple-Junction Solar Cells With 30.2% Efficiency Under 1-Sun AM1.5g. *IEEE J. Photov.* **2017**, *7*, 367−373.
(31) Shockley, W.; Queisser, H. J. Detailed Balance Limit of Efficiency of *p-n* Junction Solar Cells. *J. Appl. Phys.* **1961**, *32*, 510−519.
(32) Ghosh, D.; Ali, M. Y.; Chaudhary, D. K.; Bhattacharyya, S. Dependence of Halide Composition on the Stability of Highly Efficient All-Inorganic Cesium Lead Halide Perovskite Quantum Dot Solar Cells. *Sol. Energy Mater. Sol. Cells* **2018**, *185*, 28−35.
(33) Akkerman, Q. A.; Gandini, M.; Di Stasio, F.; Rastogi, P.; Palazon, F.; Bertoni, G.; Ball, J. M.; Prato, M.; Petrozza, A.; Manna, L. Strongly Emissive Perovskite Nanocrystal Inks for High-Voltage Solar Cells. *Nat. Energy* **2017**, *2*, 16194.
(34) Sanehira, E. M.; Marshall, A. R.; Christians, J. A.; Harvey, S. P.; Ciesielski, P. N.; Wheeler, L. M.; Schulz, P.; Lin, L. Y.; Beard, M. C.; Luther, J. M. Enhanced Mobility $CsPbI_3$ Quantum Dot Arrays for Record-Efficiency, High-Voltage Photovoltaic Cells. *Sci. Adv.* **2017**, *3*, No. eaao4204.
(35) Wheeler, L. M.; Sanehira, E. M.; Marshall, A. R.; Schulz, P.; Suri, M.; Anderson, N. C.; Christians, J. A.; Nordlund, D.; Sokaras, D.; Kroll, T.; et al. Targeted Ligand-Exchange Chemistry on Cesium Lead Halide Perovskite Quantum Dots for High-Efficiency Photovoltaics. *J. Am. Chem. Soc.* **2018**, *140*, 10504−10513.
(36) Yuan, J.; Ling, X.; Yang, D.; Li, F.; Zhou, S.; Shi, J.; Qian, Y.; Hu, J.; Sun, Y.; Yang, Y.; et al. Band-Aligned Polymeric Hole Transport Materials for Extremely Low Energy Loss α-$CsPbI_3$ Perovskite Nanocrystal Solar Cells. *Joule* **2018**, *2*, 2450−2463.
(37) Xue, J.; Lee, J.-W.; Dai, Z.; Wang, R.; Nuryyeva, S.; Liao, M. E.; Chang, S.-Y.; Meng, L.; Meng, D.; Sun, P.; et al. Surface Ligand Management for Stable $FAPbI_3$ Perovskite Quantum Dot Solar Cells. *Joule* **2018**, *2*, 1866−1878.
(38) Denton, A. R.; Ashcroft, N. W. Vegard's Law. *Phys. Rev. A: At., Mol., Opt. Phys.* **1991**, *43*, 3161−3164.
(39) Protesescu, L.; Yakunin, S.; Kumar, S.; Bär, J.; Bertolotti, F.; Masciocchi, N.; Guagliardi, A.; Grotevent, M.; Shorubalko, I.; Bodnarchuk, M. I.; et al. Dismantling the "Red Wall" of Colloidal Perovskites: Highly Luminescent Formamidinium and Formamidinium−Cesium Lead Iodide Nanocrystals. *ACS Nano* **2017**, *11*, 3119−3134.
(40) Wang, P.; Zhang, X.; Zhou, Y.; Jiang, Q.; Ye, Q.; Chu, Z.; Li, X.; Yang, X.; Yin, Z.; You, J. Solvent-controlled growth of inorganic perovskite films in dry environment for efficient and stable solar cells. *Nat. Commun.* **2018**, *9*, 2225.
(41) Savenije, T. J.; Ferguson, A. J.; Kopidakis, N.; Rumbles, G. Revealing the Dynamics of Charge Carriers in Polymer:Fullerene Blends Using Photoinduced Time-Resolved Microwave Conductivity. *J. Phys. Chem. C* **2013**, *117*, 24085−24103.
(42) Reid, O. G.; et al. Quantitative analysis of time-resolved microwave conductivity data. *J. Phys. D: Appl. Phys.* **2017**, *50*, 493002.

DOI: 10.1021/acsenergylett.9b01030
ACS Energy Lett. 2019, 4, 1954−1960